Surface & Coatings Technology 485 (2024) 130904

Contents lists available at ScienceDirect

Surface & Coatings Technology

journal homepage: www.elsevier.com/locate/surfcoat

Laser-directed energy deposition of bioactive glass on Ti-6Al-7Nb titanium alloy substrate with highly refined grain structure

Szymon Bajda [a,*], Katarzyna Cholewa-Kowalska [c], Michal Krzyzanowski [a,d], Michal Dziadek [c,e], Mateusz Kopyscianski [a], Yijun Liu [b], Adarsh Rai [a]

[a] Faculty of Metals Engineering and Industrial Computer Science, AGH University of Krakow, Mickiewicza 30, Krakow 30-059, Poland
[b] Manufacturing Technology Centre, Ansty Park, Coventry CV7 9JU, United Kingdom
[c] Faculty of Materials Science and Ceramics, AGH University of Krakow, Mickiewicza 30, Krakow 30-059, Poland
[d] Birmingham City University, Faculty Computing, Engineering & the Built Environment, Millenium Point, Curzon Street, Birmingham B4 7XG, United Kingdom
[e] Faculty of Chemistry, Jagiellonian University, Golebia 24, Krakow 31-007, Poland

ARTICLE INFO

Keywords:
Directed energy deposition
Ultrafine-grained structure
Titanium alloys
Bioactive glass
Medical implants
In vitro

ABSTRACT

The bioactive glass S520 was applied to an ultrafine-grained Ti-6Al-7Nb titanium alloy by a laser-directed energy deposition (LDED) process, in order to create a biocompatible material without potentially toxic vanadium for use in load bearing biomedical implants. The laser cladding process influenced the substrate's structure by melting the metallic material at the surface and infusing it with bioactive glass. Subsequently, the melted titanium alloy crystallised, resulting in the formation of relatively large grains. Deeper into the material, laser-induced heat triggered martensitic transformation, leading to the formation of α′ acicular martensite. In the lower regions of the HAZ, a distinctive band with refined grains was identified. Detection of certain amounts of Al directly in the bioactive glass raises concerns about potential toxicity as the glass dissolves in the human body. The nearly complete reduction in P concentration after 14 days highlights the high bioactivity of the material produced.

1. Introduction

Due to the combination of high specific strength, corrosion resistance, and biocompatibility, titanium and its alloys can be found in a wide range of biomedical applications [1]. They are commonly used as implant devices to replace damaged hard tissue. Examples of such devices include artificial hip and knee joints, bone plates, screws for fracture fixation, and pacemakers, among others [2,3]. They are also used as dental implants to replace lost teeth in patients [4–6].

The long-term implant market was previously dominated by the Ti-6Al-4V alloy. However, it was pointed out that the use of vanadium-containing alloys puts the patient's health at risk due to their negative effects, including allergy, inflammation, carcinogenicity, and other conditions [7–10]. Gradually moving away from the Ti-6Al-4V alloy in favour of vanadium-free titanium alloys comprising more biocompatible elements, such as Mo, Nb, Zr, or Ta, which are better tolerated in the tissue environment, is the result of careful monitoring of long-term implants containing toxic vanadium in the human body. The Ti-6Al-7Nb alloy, which can be used as an alternative to Ti-6Al-4V by substituting Nb for V, is of particular interest among this group of titanium alloys. Furthermore, Ti-6Al-7Nb has a higher corrosion resistance compared to the Ti-6Al-4V alloy [11,12].

Titanium and its alloys are bioinert materials, which means that they do not initiate a response or interact when introduced into biological tissue. Once placed in the human body, bioinert implants do not form chemical or biological bonds at the tissue/implant interface, which can cause relative movements that accelerate wear on their surface and stimulate inflammatory reactions [13]. It is crucial to create a reliable contact between the adjacent bone and the implant without fibrous tissue formation. This means that the prosthesis must have a suitable surface to integrate effectively with the surrounding bone [14]. One way to obtain such a surface is to cover the implant with bioactive glass material [15].

Bioactive glasses are solid and hard materials consisting of the main component SiO_2 and various additional basic components, which are usually Na_2O, CaO, MgO, P_2O_5 and K_2O. By varying any of these, different types of bioactive glasses can be obtained [16]. They are characterised by high bioactivity, osteoconduction, and

* Corresponding author.
E-mail address: sbajda@agh.edu.pl (S. Bajda).

https://doi.org/10.1016/j.surfcoat.2024.130904
Received 23 February 2024; Received in revised form 7 May 2024; Accepted 8 May 2024
Available online 10 May 2024

Table 1
The S520 bioactive glass powder's chemical composition.

	SiO_2	Na_2O	CaO	K_2O	P_2O_5
Nominal mol, %	52	20.9	18	7.1	2
mol, %	51.8	19.4	19.3	7.4	2.1
wt%	48.7	18.7	17	10.9	4.7

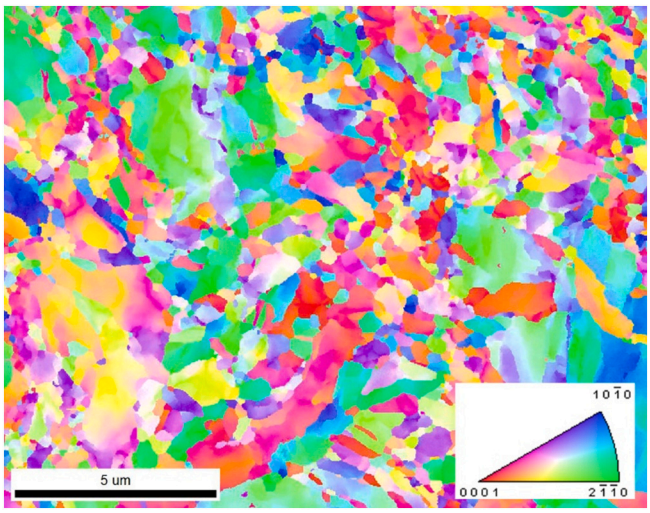

Fig. 1. A transverse cross-sectional EBSD inverse pole figure map showing the microstructure of the Ti-6Al-7Nb bar after ECAP processing.

osteostimulation, but their poor mechanical properties and brittleness limit their clinical applications to nonload-bearing implants [17]. Bioactive glasses can be used as coatings on a mechanically tough biologically inert metallic substrate to increase the fixation and osteointegration of the entire implant, where the metallic part provides high implant durability [18]. Moreover, such bioactive coatings protect the substrate from corrosion and the tissues from corrosion products that could induce adverse reactions in a human organism [19,20]. One way to apply the coating is to use laser directed energy deposition (LDED) [21].

LDED (synonym: laser cladding) is a 3D printing method that uses a focused energy source in the form of a laser beam to melt a material that is simultaneously deposited through a nozzle on a specific surface where it solidifies [22,23]. LDED is one of the most promising methods used to obtain bioactive glass coatings on metallic surfaces [24]. This technique has many advantages due to the good deposition rate and the fact that the entire substrate is not exposed to high temperatures during processing. The coatings obtained using LDED preserve the bioactivity of the original glass [25].

The microstructure of the metallic substrate on which the bioactive glass is to be clad can be refined to significantly improve its properties. It was shown that the yield and ultimate strength of commercially pure titanium (cpTi) and some of its alloys can be increased even more than twice [26–28]. Furthermore, wear resistance is significantly improved by reducing the grain size in cpTi [29,30] and other metallic materials [31,32]. The fatigue behaviour and biocompatibility of cpTi are also improved [29,33]. In addition, the grain refinement of titanium alloys reduces its corrosion rate [34,35], which can be important when alloys contain potentially harmful elements such as aluminium or vanadium [36,37]. The microstructure of metallic substrates can be refined using severe plastic deformation (SPD) processes such as equal channel angular pressing (ECAP) [38].

Recent studies have explored the application of bioactive coatings onto titanium substrates to enhance their biomedical functionalities. For instance, Kongsuwan et al. [39] achieved strong adhesion and high

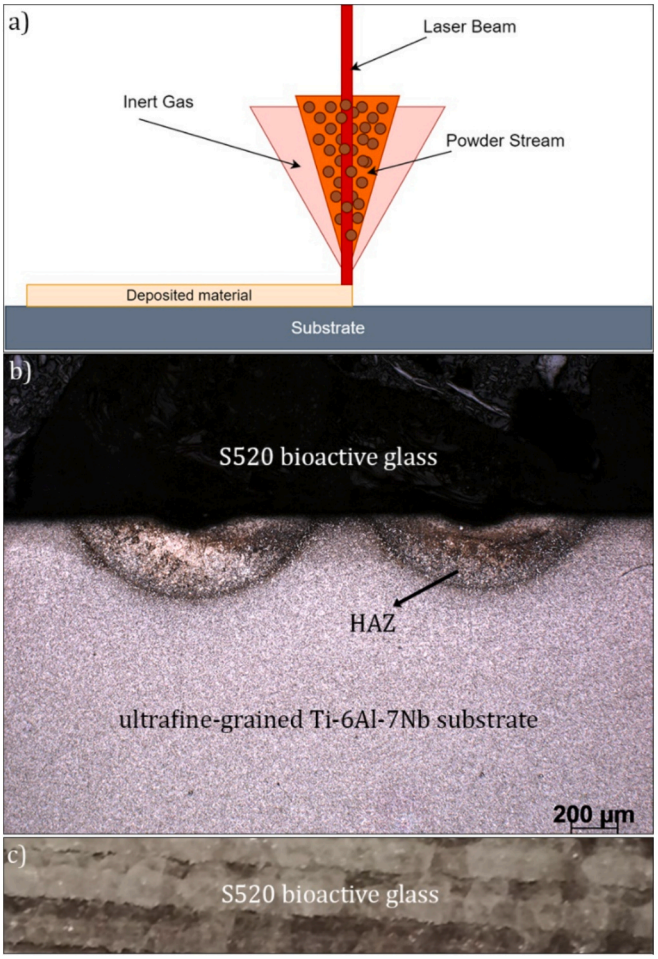

Fig. 2. a) Visual representation of the LDED process, b) cross section of multiple S520 bioactive glass tracks coated on an ultrafine-grained Ti-6Al-7Nb alloy substrate, c) top view of the S520 coating composed of multiple tracks.

bioactivity by coating grade 2 titanium substrates with 45S5 bioactive glass using continuous wave laser techniques. Comesaña et al. [25] produced bioactive glass coatings on Ti-6Al-4V titanium alloy substrates without surface pre-treatment via laser cladding. Roy et al. [40] improved cell differentiation and biomineralization by coating titanium with tricalcium phosphate (TCP) ceramics using laser-engineered net shaping (LENS™). Ke et al. [41] enhanced biological and antibacterial properties by developing a gradient coating of hydroxyapatite (HA) on Ti6Al4V substrates. In our recent work [42], we demonstrated high bioactivity in vitro by laser-cladding bioactive glass coating S520 onto a commercially pure titanium (cpTi) substrate with highly refined grain structure. However, previous studies have primarily focused on conventional titanium alloys for biomedical applications. Notably, our study pioneers the utilization of an ultrafine-grained titanium alloy, which may present improved mechanical properties and biocompatibility, thus potentially enhancing its suitability for load-bearing biomedical implants.

In this study, we coated the ultrafine-grained Ti-6Al-7Nb titanium alloy substrate with bioactive glass S520 to develop a biocompatible material suitable for load-bearing biomedical implants, thereby eliminating potentially toxic vanadium. The main objectives of this work were as follows:

- to investigate the feasibility of using LDED to coat bioactive glass onto a titanium alloy substrate with highly refined grain structure,
- to evaluate the microstructural changes induced by the LDED process on the substrate material,

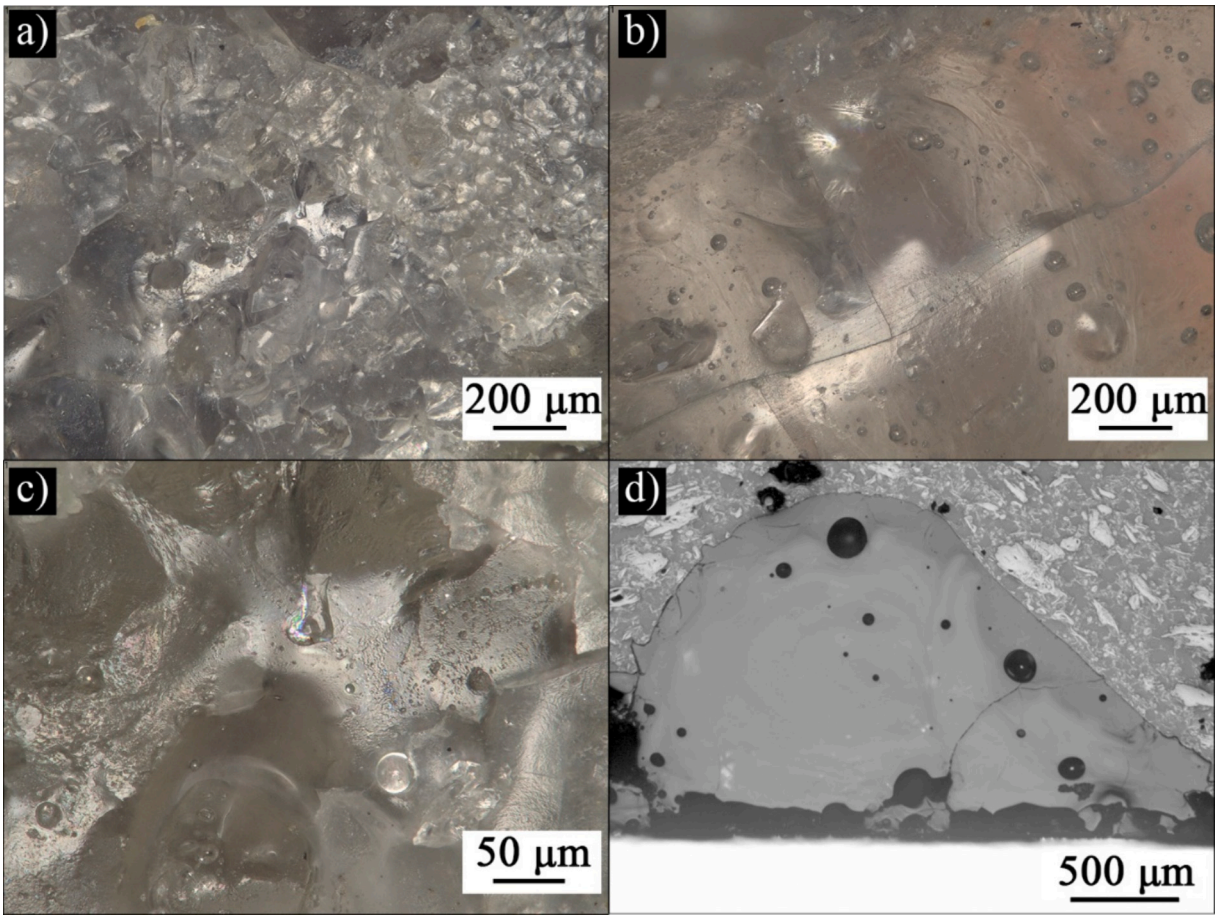

Fig. 3. a–c) Top-view images and b) cross-sectional optical micrograph showing the S520 bioactive glass coating.

- to assess the bioactivity of the obtained biocompatible material for potential biomedical applications,
- to investigate the presence of potentially toxic aluminium within the bioactive glass coating.

2. Materials and methods

2.1. Bioactive glass

The S520 powder was selected because it exhibits a relatively smooth wetting angle temperature behaviour and has already been used to produce bioactive glass coatings using the LDED process [25,42].

The melt-quenching technique was used to produce the S520 bioactive glass powder with the composition shown in Table 1. Using a SpeedMixer (FlackTekInc, USA), the glass batch was prepared by combining the appropriate amounts of silicon dioxide (SiO_2, AR, POCh, Poland), sodium carbonate (Na_2CO_3, AR, POCh, Poland), calcium carbonate ($CaCO_3$, AR, POCh, Poland), potassium carbonate (K_2CO_3, AR, POCh, Poland) and phosphorus pentoxide (P_2O_5, AR, Sigma-Aldrich).

A platinum crucible was used to melt the homogenised powder in an electric furnace for two hours at 1450 °C. The molten glass was poured into cold water to obtain glass frit, which was then dried to a constant weight. The glass frit was milled using a zirconia grinding bowl and ball in a planetary mill (Pulverisette 6, Fritsch) and sieved to obtain bioactive glass powder with particle sizes between 100 and 200 µm.

A more detailed characterisation of the powder obtained is given in our previous work [42].

2.2. Bioinert substrate

The ultrafine-grained Ti-6Al-7Nb titanium alloy was obtained and supplied by the Institute of Physics of Advanced Materials (Ufa State Aviation Technical University, Russia). The alloy was produced using the ECAP process [43,44]. The obtained metallic bar had a cross-sectional area of 11 mm × 11 mm, and its microstructure is shown in Fig. 1. The micrograph illustrates that most grains have a diameter below 1 µm. However, there are also individual grains that are several times larger in size.

2.3. Cladding of bioactive glass powder onto a bioinert substrate using LDED

A slow-speed diamond saw was used to cut ultrafine-grained Ti-6Al-7Nb titanium alloy bars in half along the longitudinal section. Before LDED, acetone was used to clean the surface of the titanium sample. Then, the synthesised bioactive glass S520 was clad onto an ultrafine-grained titanium alloy substrate using the same laser cladding (LDED) technique as in our recent work [42]. Fig. 2a presents an illustrative diagram explaining the LDED process. The employed hybrid LDED system is composed of a 5-axis Mikron 450u machine, which has been combined with a modified laser deposition system and a multi-material powder delivery system. The laser used emits light at a fundamental wavelength of 1064 nm and can generate a maximum output power of 1200 W. To deliver the powder, high-purity argon gas was employed, both as the carrier gas for the powder and as the shielding gas on the sides. To maintain continuous powder flow and protect the titanium substrate from oxidation, the volumetric flow rates of the powder-carrying gas and the shielding gas were adjusted to approximately 2

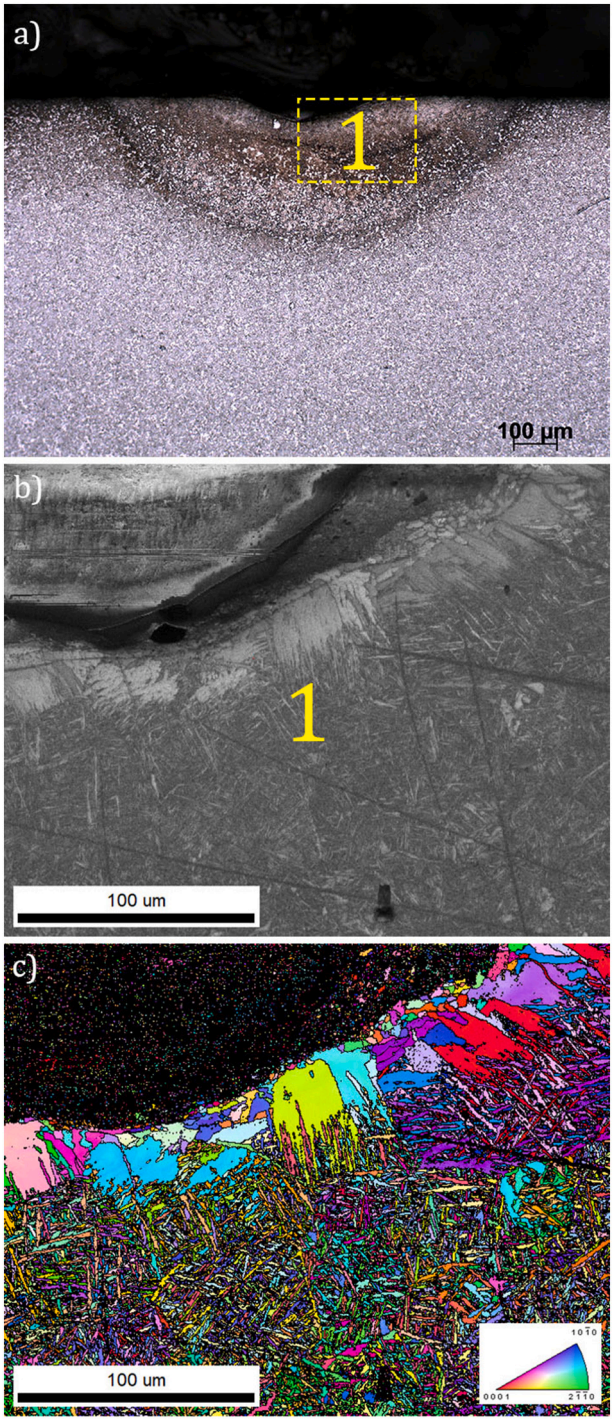

Fig. 4. a) Cross section of a single-track bioactive glass S520 coated on an ultrafine-grained Ti-6Al-7Nb substrate, b) SEM image of an enlarged region marked "1" in figure (a), c) EBSD scan of the same region.

to 5 l/min and 5 to 10 l/min, respectively.

The laser beam was concentrated on the surface of the substrate with a focal length of 50 mm, resulting in a laser spot size of 1 mm in diameter. The working head, comprising laser optics and a powder injection system, was assembled and securely positioned, while the substrate moved at a scanning speed of 1.5 mm/s, with the laser operating at 50 W. We experimented with various laser power levels up to 100 W, and we found that 50 W was the optimal level for our purposes. At this power level, we observed that the laser stability was sufficient for producing the small samples required for our study. The power density was

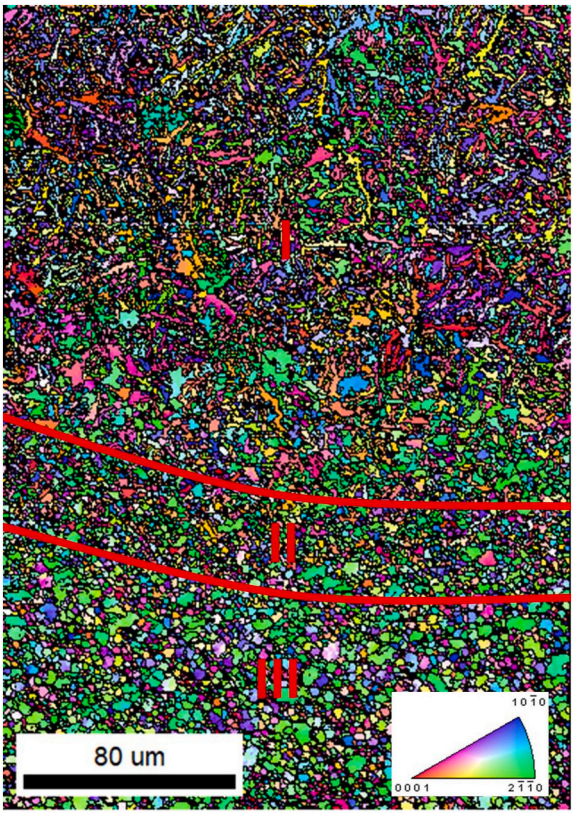

Fig. 5. EBSD cross section scan of the Ti-6Al-7Nb microstructure at approximately 100–400 µm below the bioactive glass. I, II, III – zone markers.

measured at 6369 W/cm^2. To ensure smooth flow throughout the process, bioactive glass powder particles sized between 100 and 200 µm were chosen. Multiple adjacent bioactive tracks of S520 were clad with approximately a 25 % overlap, forming a coating (Fig. 2b–c).

2.4. Material characterisation

Ultrafine-grained bioactive glass-coated Ti-6Al-7Nb samples were carefully sectioned using a low-speed diamond saw to prevent stress-induced cracking. Subsequently, these samples were initial ground on abrasive paper (SiC) and then mechanically polished on cloths to prepare them for microstructure analysis. The samples were subjected to examination using both light microscopy and scanning electron microscopy (SEM) with backscattered electrons for imaging and diffraction (EBSD). Additionally, chemical analysis was conducted through energy-dispersive X-ray spectroscopy (EDS mapping) within the SEM. All microstructural investigations were performed using a Zeiss Axio Imager M1m light microscope, a Keyence VHX-7000 digital microscope and a high-resolution FEI Nova NanoSEM scanning electron microscope, which featured a field emission gun and an EDAX system for chemical analysis.

We measured the hardness of the sample cross sections using a Vickers microhardness tester, applying a 50 g indentation load for a dwell time of 10 s. We made sure to maintain a distance of at least 20 µm between the adjacent indentations to avoid any inaccuracies caused by the affected plastic zone near the indentation.

2.5. In vitro studies

The investigation of the in vitro bioactivity followed the method outlined in [45]. The samples, which originally exceeded a length of 100 mm following the laser cladding process, needed to be divided into smaller sections prior to immersion in simulated body fluid (SBF) for

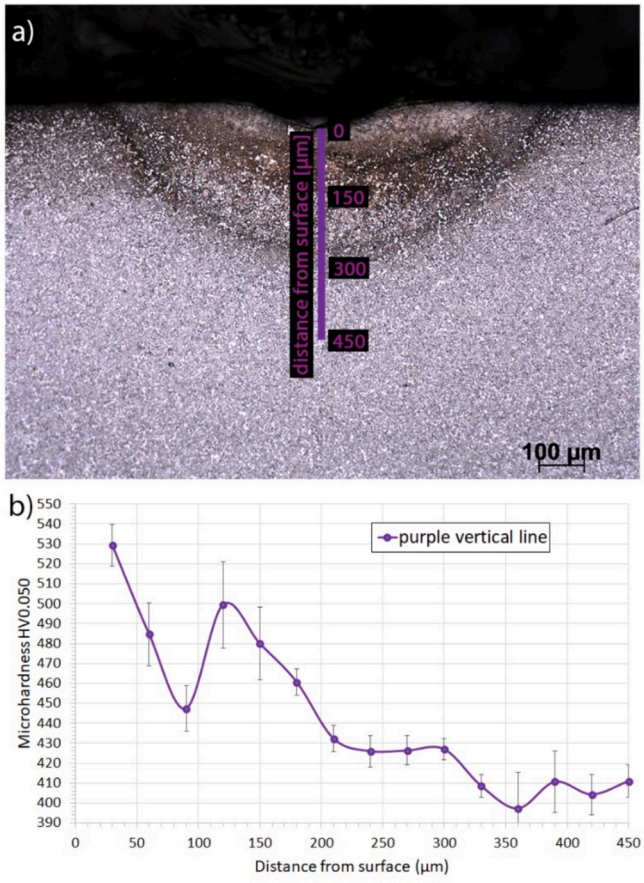

Fig. 6. Changes in cross-sectional Vickers microhardness beneath the cladded bioactive glass track, a) indicates the purple line marked on the optical micrograph, representing the path where hardness measurements were conducted, and b) illustrates the variation in microhardness across the depth.

further analysis. To facilitate the cutting process, we applied a protective resin coating over the bioactive glass layer. However, removing this resin for testing purposes was a complex procedure that could potentially affect the texture and structure of the bioactive glass or even cause damage to the coatings themselves, thereby affecting the test results. Because the primary objective of the experiments was to evaluate the bioactivity of the coating post-laser cladding, the decision was made to separate the cladded layer from the titanium alloy basement. As a result, portions of the bioactive glass were removed from the ultrafine-grained Ti-6Al-7Nb substrate. These glass fragments were then immersed in SBF and kept at 37 °C for 3 and 14 days, with a weight-to-volume ratio of 1/100 between the glass sample and the solution. Subsequently, the samples were removed from the SBF, washed in pure ethanol, and left to air dry at 25 °C.

Before and after the bioactivity test, the structure of the samples was analysed using FTIR and Raman spectroscopy. FTIR spectra were obtained using the Bruker Vertex 70v spectrometer. Samples, including glass powder and coating, were prepared using the standard KBr pellet method. Spectra were recorded in the mid-infrared range (4000 to 400 cm^{-1}), and 128 scans were averaged at a resolution of 4 cm^{-1}. Raman analysis was performed using the Horiba LabRAM HR micro-Raman spectrometer. A 532-nm laser with a power of 15 mW was employed. The 1800 g/mm grating with 100× objectives was used and 2 scans of 300 s each were accumulated.

We examined the surface morphology and performed chemical analysis on the samples both before and after mineralisation in SBF. This analysis was carried out using SEM with a Nova NanoSEM 200 FEI Europe Company instrument, operating at an accelerating voltage of 15 kV. We also used an energy dispersion X-ray (EDX) analyser. Furthermore, we monitored changes in calcium (Ca), phosphorus (P), and silicon (Si) concentrations in SBF during sample immersion using the ICP-OES technique with a Plasm 40 instrument (Perkin Elmer, USA).

3. Results and discussion

3.1. Bioactive glass coating

The morphology of S520 bioactive glass coated on an ultrafine-grained Ti-6Al-7Nb substrate is shown in Fig. 3. The top-view image of the coating in Fig. 3a indicates rough surface, while Fig. 3b and 3c show a relatively smooth area, but both have an amorphous microstructure. Therefore, it can be concluded that the morphology of the glass coating is not uniform. Fig. 3d shows the cross-section of the coating, revealing pores of various sizes, although their volume fraction is not significant. Additionally, some visible cracks are observed in the glass.

3.2. Microstructure

Fig. 4a shows an optical micrograph of a cross section that reveals the area containing the heat affected zone (HAZ) below the bioactive glass coating. Notably, significant microstructure changes are apparent below the coating, primarily due to the thermal effects of the laser. However, it is important to note that the optical micrograph does not capture all the microstructure changes resulting from the heat influence. These changes extend to depths greater than what is shown on the optical micrograph. Additional techniques, such as SEM and EBSD, are necessary for their identification. The visible HAZ has a width of approximately 970 µm and a depth of approximately 345 µm. In the upper part of this zone, the horizontal boundary between glass/metal undergoes bending, resulting from the strong laser interaction with this area, leading to metal melting and the filling of this area with bioactive glass. The width of this zone is approximately 320 µm, and its depth is approximately 55 µm. The shape of this zone and that of the entire visible HAZ is quite characteristic. The depth of the zones increases as one approaches their centres. This shape results from the Gaussian distribution of the laser beam intensity. A dashed-line rectangle is used to mark a rectangular area that covers a section of the bioactive glass, which now occupies the space where the metal was previously located. This rectangle, marked with number 1, also includes areas situated at greater depths. SEM (Fig. 4b) and EBSD (Fig. 4c) analyses were conducted in the indicated region.

Fig. 4b shows a cross-sectional SEM view, where bioactive glass and a Ti-6Al-7Nb alloy underneath it are visible. Directly beneath the glass, one can observe large grains with diameters ranging in the tens of micrometres. These grains resulted from crystallisation within the liquid phase induced by laser interaction. The EBSD image (Fig. 4c) reveals that below these large grains, significantly smaller grains with elongated shapes can be observed. We identified them as α′ acicular martensite. We found a similar martensitic structure in cpTi after laser cladding of bioactive glass on its surface [42]. It was also identified after laser surface remelting of a commercially pure titanium sheet by Sun et al. [46]. α′ martensite is also found in the Ti-6Al-7Nb alloy produced through the selective laser melting (SLM) process [47].

An additional EBSD scan was taken at a greater depth, within the range of approximately 100 µm to 400 µm below the bioactive glass (Fig. 5). The image shows an area covering the part of the HAZ that is visible in Fig. 4a, as well as the region below. Three zones can be distinguished in the image. In the upper part of fig. (I), acicular martensite grains similar to those seen in Fig. 4c can be observed. Below, there are fine equiaxed grains, with diameters typically falling within the range of 1–2 µm. The width of this zone (II) measures approximately 30–40 µm, corresponding to the width of the lower band visible in Fig. 4a. Below this band lies Zone III, where equiaxed grains dominate, with diameters larger by several tens of percent compared to the grains

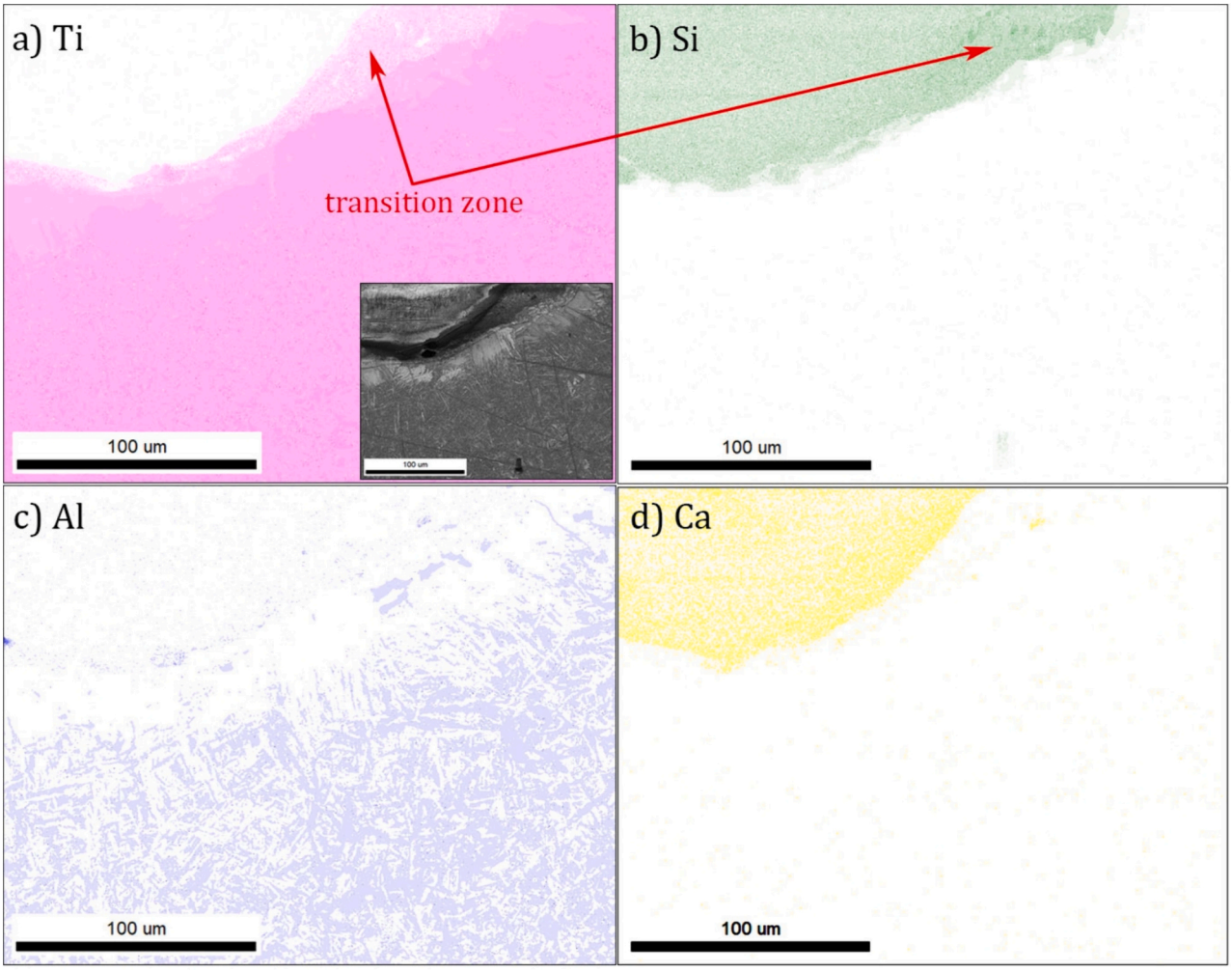

Fig. 7. EDS elemental mapping from the interface area of bioactive glass with a metallic substrate, as visible in Fig. 4b, a) Ti, b) Si, c) Al, d) Ca.

in Zone II. It should be noted that HAZ has affected the entire microstructure visible on the EBSD scan, since the grains after the ECAP process were considerably smaller, typically with diameters less than 1 μm (Fig. 1).

3.3. Microhardness

The ultrafine-grained Ti-6Al-7Nb sample cross section was subjected to hardness evaluation using the Vickers micro-hardness tester. The core hardness of the substrate was found to be around 410 HV, which is approximately 100 HV higher than that of ultrafine-grained cpTi [42]. The optical micrograph, shown in Fig. 6a, shows a HAZ zone in which a purple vertical line was plotted. In this area, hardness measurements were carried out. The values obtained were averaged after three indentations were made at identical depths below the surface.

The greatest hardness was detected slightly beneath the metal surface, measuring approximately 530 HV at a depth of 30 μm - this marks around a 30 % increase compared to the core hardness. According to the EBSD scan (Fig. 4c), α′ acicular martensite is visible below a depth of approximately 20 μm. Its presence might explain the higher values observed compared to the core, as it inherently possesses superior hardness [46]. From there, the hardness gradually decreases until it reaches approximately 90 μm in depth, where it begins to rise again. For ultrafine-grained cpTi, the hardness values were lower than its core hardness until approximately 150 μm in depth. However, similar to the ultrafine-grained Ti-6Al-7Nb substrate, the values directly below the surface were higher compared to those at 90 μm depth. The hardness begins to rise at a depth of approximately 90 μm, climbing from about 450 to approximately 500 HV at 125 μm deep. Subsequently, it gradually declines to around 425 HV at a depth of approximately 220 μm. The hardness values remain relatively consistent until a depth of approximately 300 μm, where the hardness begins to decrease and reaches about 30 HV less at a depth of around 360 μm. In the micrograph (Fig. 6a) at a depth of about 300 μm, noticeable changes in the microstructure are visible: there is a characteristic arc-shaped band formed as a result of the laser beam interaction. The location of this band corresponds to the Zone II seen in the EBSD image (Fig. 5), located at a depth of approximately 280–330 μm. The decrease in hardness of the approximately 30 HV mentioned above occurs within this zone. This could be due to the absence of martensite observed in this area. Below the depth of approximately 330 μm, the hardness values fluctuate around 410 HV, which represents the core hardness.

3.4. Chemical analysis

EDS analysis was performed in the contact area between bioactive S520 glass and the metallic Ti-6Al-7Nb substrate (Fig. 7). Note that EDS spectroscopy may not be sensitive enough to detect smaller amounts of the relevant elements.

A transition zone was identified between the metallic material and the glass in which the elements Ti, Al, and Si appeared. This is likely because the material in this area underwent melting, significantly facilitating its flow. Ti elements were not directly identified in the glass itself. After applying the same bioactive glass to an ultrafine-grained

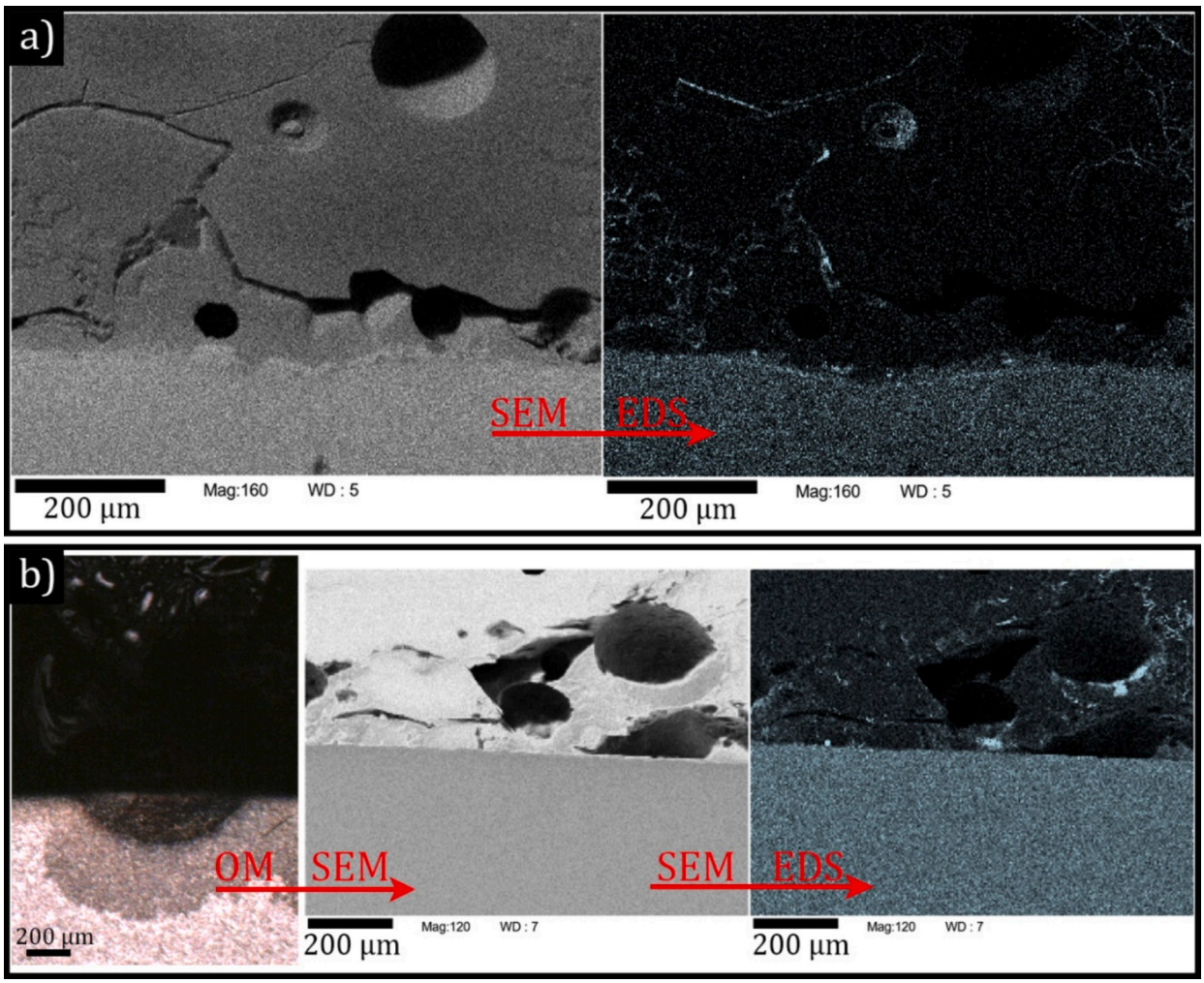

Fig. 8. a) A cross-sectional SEM image from the bioactive glass interface area with a metallic substrate (left) and EDS elemental mapping of Al from this region (right), b) a cross-sectional optical micrograph of the interface area between the bioactive glass and the metallic substrate, where no glass infusion into the substrate occurred due to the melting of the titanium alloy (left) along with a cross-sectional SEM image from this interface area (middle) with EDS elemental mapping of Al from this region (right).

pure titanium substrate, Ti elements were also not detected in the clad layer [42]. Comesaña et al. [25], who used laser cladding to produce a bioactive glass S520 coating on a Ti-6Al-4V substrate, also did not find any Ti in the glass coating by EDS analysis. Si and Ca were not observed in the Ti-6Al-7Nb substrate.

Certain amounts of Al were detected directly in the bioactive glass. To confirm these results, an additional EDS analysis was performed, this time in a different area of the glass-metal interface, as shown in Fig. 8a. It can be observed that Al is present throughout the entire cross section of the glass. Kuo et al. [48] used laser cladding to apply 45S5 bioactive glass to a Ti6Al4V substrate and performed an EDS analysis to acquire elemental distribution within the cross-sectional area of the bioactive glass coated Ti-6Al-4V alloy. Their findings revealed an approximate 30 % presence of Al in the bioactive glass coating, around 20 µm above the interface. This observation indicated a significant transfer of Al into the bioactive glass, potentially posing toxicity concerns as the glass dissolves within the human body. Furthermore, the increasing presence of substrate elements within the coating resulted in a reduction of the average content of Na and P in the bioactive glass, ultimately reducing its overall bioactivity. Additionally, to confirm that the presence of Al in the coating does not result from its evaporation from the metallic substrate, another EDS analysis was conducted (Fig. 8b). However, this time, the area selected for examination was the interface between the bioactive glass and the metallic substrate, where no glass infusion into the substrate is seen, suggesting that the melting of the alloy did not occur. This indicates that the temperatures resulting from the laser irradiance were lower in this region, preventing Al from evaporating. Nevertheless, the EDS analysis showed the presence of aluminium in the coating (Fig. 8b, image on the right).

It is believed that the presence of Al in the coating is primarily attributed to the oxidation reaction of Al with oxides such as Na_2O, CaO, etc., forming more stable Al_2O_3 due to its higher enthalpy compared to other oxides. This is also mentioned elsewhere [49].

3.5. *In vitro study*

Raman and Fourier-transform infrared (FTIR) spectroscopic techniques were employed to investigate the changes in the structural characteristics of bioactive glass S520 after laser cladding and a 14-day immersion in SBF (Fig. 9). We further compared the acquired results with the results we obtained for the glass applied to an ultrafine-grained cpTi substrate [42].

Before being submerged in SBF, no differences were observed between the Raman spectra obtained for the S520 glass and the coating on the ultrafine-grained cpTi substrate (Fig. 9a). Two wide bands associated with Si–O–Si were detected at 600–620 cm^{-1} (rocking) and 1050–1080 cm^{-1} (stretching). Another band is visible at 940–950 cm^{-1}, which is attributed to the presence of non-bridging oxygen (NBO) in

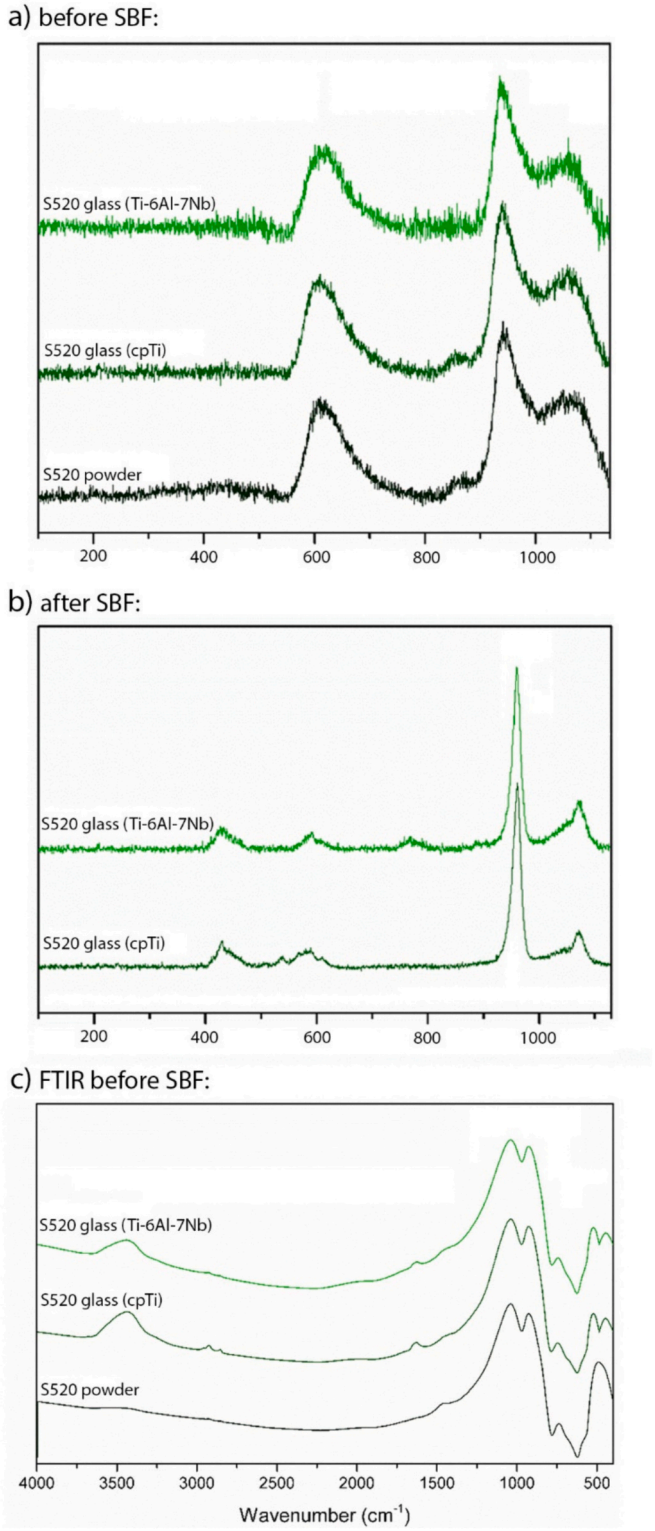

Fig. 9. Raman spectra of the bioactive glass powder and the bioactive glass coated on the ultrafine-grained Ti-6Al-7Nb and cpTi substrates before (a) and after (b) a 14-day immersion in SBF, as well as the FTIR spectra taken before immersion in SBF (c).

Si–O(NBO). Del Val et al. [50] performed laser cladding of S520 bioactive glass to create three-dimensional multilayered glass implants. They used varying laser parameters, specifically using a wavelength of $\lambda = 1.6$ μm and a laser power of 18 W, and the observed results were very similar.

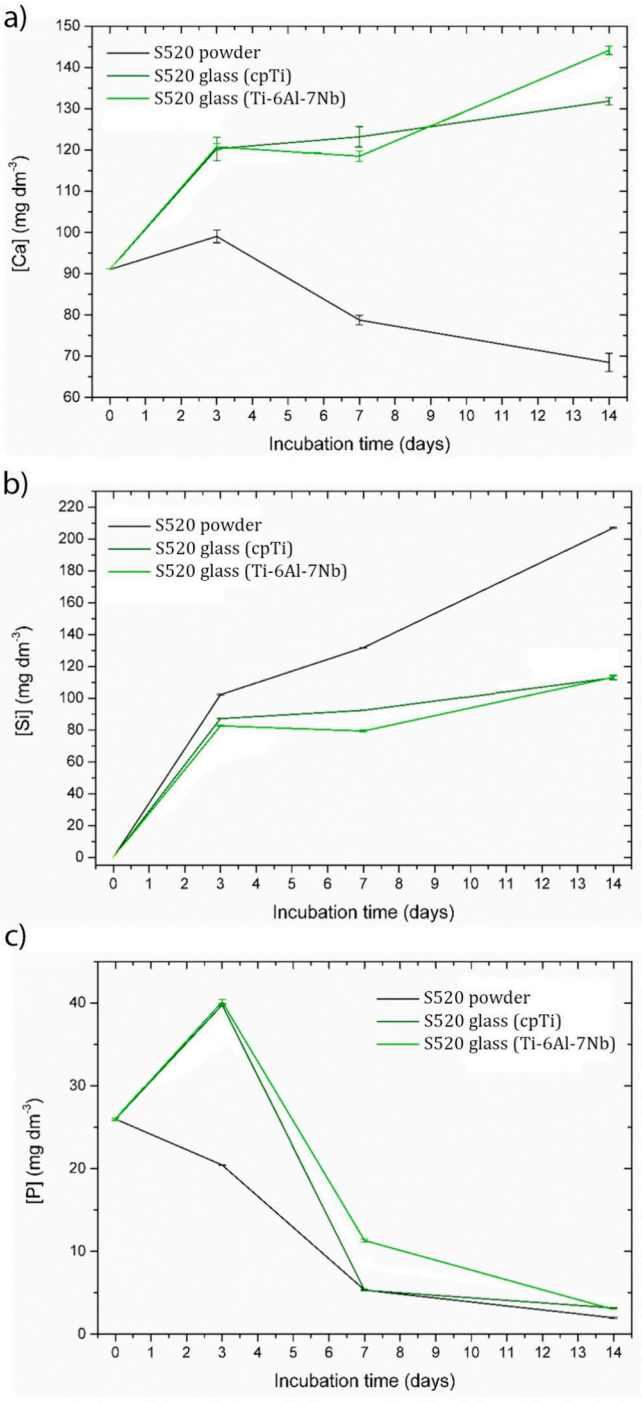

Fig. 10. Ca (a), Si (b) and P (c) concentration with the SBF incubation time for bioactive glass powder and bioactive glass coated on ultrafine-grained Ti-6Al-7Nb and cpTi substrates.

Raman spectra specific for HA were observed after a 14-day incubation of the material in SBF (Fig. 9b). These spectra did not display any characteristic bands typically associated with glass, indicating a tight cover of the analysed materials by the HA layer. The presence of the HA layer was confirmed by the emergence of new bands in the Raman spectra, mainly a prominent band at 945–965 cm^{-1}, originating from the symmetric stretching vibration ($\nu 1$) of the P—O bond within the [PO_4] groups in crystalline HA. In addition to the main peak at 945–965 cm^{-1}, the P—O asymmetric stretching was also evident in the band at 1065–1075 cm^{-1}, along with a shoulder at 1020–1065 cm^{-1}. The

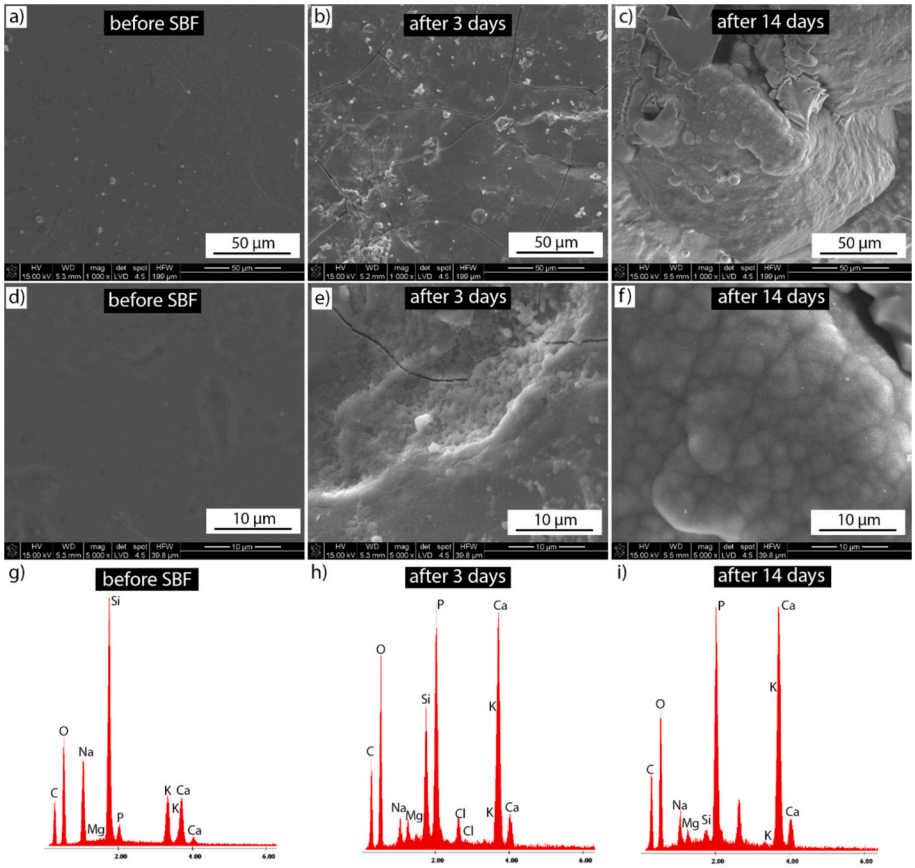

Fig. 11. SEM images (a–f) and EDS spectrum of bioactive glass coated onto the ultrafine-grained Ti-6Al-7Nb substrate before (a, d, g), after 3 (b, e, h) and after 14 (c, f, i) days of immersion in SBF.

presence of the band at 1065–1075 cm^{-1} can also be attributed to the symmetric stretching mode ($\nu 1$) in the [CO_3] group, suggesting carbonate substitution within the anionic substructure of the crystallised HA. Furthermore, the bands within the ranges of 430–450 cm^{-1} and 565–610 cm^{-1} ranges, which correspond to the bending modes of the P—O ($\nu 2$) and O–P–O ($\nu 4$) bonds within the [PO_4] groups, respectively, indicate the crystallisation of HA.

The FTIR spectra for S520 bioactive glass coatings and powder are shown in Fig. 9c. Significant differences between powder and the coatings are mostly observed in the 450–600 cm^{-1} region, and the coatings applied to different substrates did not show noticeable variations in their spectra. The stretching vibration modes of Si—O and Si–O (2NBO) are represented by two bands, which are located at about 1030–1060 cm^{-1} and 900–930 cm^{-1}, respectively. These bands are consistent with the results of Comesaña et al. [51], who used laser cladding to create three-dimensional structures composed of S520 bioactive glass, and Lusquiños et al. [52], who coated coarse-grained Ti-6Al-4V alloy substrates with S520 bioactive glass. Comesaña et al. [25] used a laser cladding process in another study to produce S520 coatings on substrates made of the titanium alloy Ti6Al4V. In this particular case, crystallisation caused the broad band at 1050 cm^{-1} to split into two peaks; this phenomenon was not observed in our investigation, indicating a lower degree of crystallisation. On the contrary, a single broad band indicating Si–O–Si (bend) was visible in the range of 460 to 540 cm^{-1} in the case of the bioactive glass powder S520. This band split into two separate bands after laser cladding, one at 450–470 cm^{-1} and the other at 510–525 cm^{-1}. This could be assigned to the formation of a crystalline phase [53].

The incubation fluid was subjected to analysis using the inductively coupled plasma optical emission spectrometer (ICP- OES), and the results are shown in Fig. 10.

An HA layer forms on the surface after a 14-day incubation period, as indicated by changes in the P concentration in SBF (Fig. 10c). Incorporation of P in the HA layer lowers the concentration of P in the solution. After 14 days, a nearly total drop in P content suggests that the materials are highly bioactive. The ion release profile is consistent with the research published in [50]. Ca levels increased significantly, indicating that the glass dissolved quickly (Fig. 10a). The creation of the HA layer is indicated by a slowdown in the release of Ca into solution after three days (inhibition of glass dissolution, inclusion of Ca into the layer). Another indication that the HA layer has formed and prevents further glass dissolution is the slowdown in the release of Si to the incubation fluid (Fig. 10b). The kinetics of changes in Ca, P, and Si concentrations in SBF between S520 glass powder and coating varied, indicating differences in sample form (bulk/powder) and consequently surface development. There are no significant differences in concentration variations for the ultrafine-grained Ti-6Al-7Nb and cpTi substrates.

The behaviour of bioactive glass coated on an ultrafine-grained Ti-6Al-7Nb substrate after immersion in SBF has been evaluated by SEM and EDS analysis (Fig. 11). A calcium phosphate (CaP) layer forms after just three days of incubation for the bioactive glass coating, according to the SEM examination (Fig. 11b, e). During incubation, an evident change in the morphology of the developing CaP layer occurs. After 14 days, the typical HCA cauliflower shapes are visible (Fig. 11c, f). The EDS spectrum of the bioactive glass material (Fig. 11g–i) illustrates a substantial decrease in Si content with increasing immersion time in the SBF. A reduction in the quantity of Na is also observed. Moreover, there is a marked increase in P and Ca levels after 3 and 14 days of immersion. A minor presence of Na and Mg is identified within the apatite layer. Comesaña et al. [25], who used laser cladding to produce the bioactive glass coating S520 on a conventional Ti-6Al-4V alloy, similarly conducted EDS analysis on the clad material. Their samples, immersed for 2

days, exhibited a high content of O, Ca, P, and Si on the surfaces. After 5 days, the coating surface was completely covered by an apatite layer, with no Si content detected. Furthermore, trace amounts of Na, Mg, and Cl were detected within the apatite layer. Peddi et al. [54] used an enameling technique to create adherent borate glass coatings on the Ti-6Al-4V alloy and conducted EDS analysis, revealing the formation of a calcium phosphate-rich layer on the glass coating surface.

4. Conclusions

The application of bioactive glass S520 on an ultrafine-grained Ti-6Al-7Nb titanium alloy through LDED has demonstrated the potential to create a biocompatible material suitable for biomedical load bearing implants without the use of toxic vanadium. The laser cladding process had a profound impact on the substrate's structure by inducing the melting of the metallic material at the surface and infusing it with bioactive glass. This process led to crystallisation, resulting in the formation of relatively large grains within the melted titanium alloy. Deeper in the material, laser-induced heat initiated a martensitic transformation, leading to the formation of α' acicular martensite. In the lower regions of the HAZ, a distinctive band with refined grains was observed. The detection of certain amounts of Al directly in the bioactive glass raises concerns regarding potential toxicity as the glass dissolves in the human body. This aspect warrants further investigation and consideration in the development of biomedical materials. Furthermore, the study identified a transition zone between the metallic material and the glass, where the elements Ti, Al, and Si were present. After 14 days of in vitro tests with the SBF solution, the samples exhibited the formation of cauliflower-shaped spherical forms, characteristic of the morphology of hydroxyapatite (HCA), indicating the high bioactivity of the bioactive glass coating. Additionally, the nearly complete reduction in P concentration after this period further emphasises the material's high bioactivity.

CRediT authorship contribution statement

Szymon Bajda: Writing – original draft, Project administration, Investigation, Funding acquisition, Conceptualization. **Katarzyna Cholewa-Kowalska:** Visualization, Validation, Methodology, Investigation. **Michal Krzyzanowski:** Supervision, Methodology, Investigation, Conceptualization. **Michal Dziadek:** Visualization, Methodology, Investigation. **Mateusz Kopyscianski:** Visualization, Methodology, Investigation. **Yijun Liu:** Methodology, Investigation. **Adarsh Rai:** Methodology, Investigation.

Declaration of competing interest

The authors declare that they have no known competing financial interests or personal relationships that could have appeared to influence the work reported in this paper.

Data availability

Data will be made available on request.

Acknowledgements

The support from the National Science Centre, Poland (grant no. DEC-2016/21/N/ST8/00091) is greatly appreciated. The authors also thank Tomasz Tokarski for his assistance in preparing the materials. We would also like to express our gratitude to Irina P. Semenova and Aleksandr V. Polyakov for preparing and providing the samples.

References

[1] P. Pesode, S. Barve, S.V. Wankhede, D.R. Jadhav, S.K. Pawar, Titanium alloy selection for biomedical application using weighted sum model methodology, Mater Today Proc 72 (2023) 724–728, https://doi.org/10.1016/j.matpr.2022.08.494.
[2] C.N. Elias, J.H.C. Lima, R. Valiev, M.A. Meyers, Biomedical applications of titanium and its alloys, JOM 60 (2008) 46–49, https://doi.org/10.1007/S11837-008-0031-1.
[3] B. Liu, Z. Deng, D. Liu, Preparation and properties of multilayer Ca/P bio-ceramic coating by laser cladding, Coatings 11 (2021) 891, https://doi.org/10.3390/coatings11080891.
[4] D. Rittel, K. Shemtov-Yona, R. Lapovok, Random spectrum fatigue performance of severely plastically deformed titanium for implant dentistry applications, J. Mech. Behav. Biomed. Mater. 83 (2018) 94–101, https://doi.org/10.1016/J.JMBBM.2018.04.012.
[5] J.W. Nicholson, Titanium alloys for dental implants: a review, Prosthesis 2020, Vol. 2, Pages 100–116 2 (2020) 100–116. doi:https://doi.org/10.3390/PROSTHESIS2020011.
[6] M. Saini, Y. Singh, P. Arora, V. Arora, K. Jain, Implant biomaterials: a comprehensive review, World Journal of Clinical Cases : WJCC 3 (2015) 52, https://doi.org/10.12998/WJCC.V3.I1.52.
[7] M. Kaur, K. Singh, Review on titanium and titanium based alloys as biomaterials for orthopaedic applications, Mater. Sci. Eng. C 102 (2019) 844–862, https://doi.org/10.1016/j.msec.2019.04.064.
[8] J. Willis, S. Li, S.J. Crean, F.N. Barrak, Is titanium alloy Ti-6Al-4V cytotoxic to gingival fibroblasts—a systematic review, Clin Exp Dent Res 7 (2021) 1037–1044, https://doi.org/10.1002/cre2.444.
[9] I. Zwolak, Vanadium carcinogenic, immunotoxic and neurotoxic effects: a review of in vitro studies, Toxicol Mech, Methods 24 (2014) 1–12, https://doi.org/10.3109/15376516.2013.843110.
[10] F. Peat, R. Coomber, A. Rana, A. Vince, Vanadium allergy following total knee arthroplasty, BMJ Case Rep. 2018 (2018) bcr-2017-222092. doi:https://doi.org/10.1136/bcr-2017-222092.
[11] N.A. Al-Mobarak, A.A. Al-Swayih, F.A. Al-Rashoud, Corrosion behavior of Ti-6Al-7Nb alloy in biological solution for dentistry applications, Int. J. Electrochem. Sci. 6 (2011) 2031–2042.
[12] B. Burnat, M. Walkowiak-Przybyło, T. Błaszczyk, L. Klimek, Corrosion behaviour of polished and sandblasted titanium alloys in PBS solution, Acta Bioeng. Biomech. 15 (2013) 87–95, https://doi.org/10.5277/abb130111.
[13] N. Eliaz, Corrosion of metallic biomaterials: a review, Materials 12 (2019) 407, https://doi.org/10.3390/ma12030407.
[14] K. Moghadasi, M.S. Mohd Isa, M.A. Ariffin, M.Z. Mohd Jamil, S. Raja, B. Wu, M. Yamani, M.R. Bin Muhamad, F. Yusof, M.F. Jamaludin, M.S. bin Ab Karim, B. binti Abdul Razak, N. bin Yusoff, A review on biomedical implant materials and the effect of friction stir based techniques on their mechanical and tribological properties, J. Mater. Res. Technol. 17 (2022) 1054–1121, https://doi.org/10.1016/J.JMRT.2022.01.050.
[15] J.R. Jones, Review of bioactive glass: from Hench to hybrids, Acta Biomater. 9 (2013) 4457–4486, https://doi.org/10.1016/J.ACTBIO.2012.08.023.
[16] C. Arts, J. Geurts, Management of Periprosthetic Joint Infections (PJIs), Elsevier, 2017.
[17] H. Ylänen, Bioactive Glasses: Materials, Properties and Applications, Elsevier, 2018, https://doi.org/10.1016/C2015-0-05462-4.
[18] P.P. Singh, K. Dixit, N. Sinha, A sol-gel based bioactive glass coating on laser textured 316L stainless steel substrate for enhanced biocompatability and anti-corrosion properties, Ceram. Int. 48 (2022) 18704–18715, https://doi.org/10.1016/J.CERAMINT.2022.03.144.
[19] J. Anne N. Oliver, Y. Su, X. Lu, P.H. Kuo, J. Du, D. Zhu, Bioactive glass coatings on metallic implants for biomedical applications, Bioact Mater 4 (2019) 261–270, https://doi.org/10.1016/j.bioactmat.2019.09.002.
[20] M. Krzyzanowski, S. Bajda, Y. Liu, A. Triantaphyllou, W. Mark Rainforth, M. Glendenning, 3D analysis of thermal and stress evolution during laser cladding of bioactive glass coatings, J. Mech. Behav. Biomed. Mater. 59 (2016) 404–417, https://doi.org/10.1016/j.jmbbm.2016.02.023.
[21] I. Gibson, D. Rosen, B. Stucker, Directed energy deposition processes, Additive Manufacturing Technologies (2015) 245–268, https://doi.org/10.1007/978-1-4939-2113-3_10.
[22] A.K. Praharaj, J.K. Chaurasia, G.R. Chandan, S. Bontha, P.S. Suvin, Enhanced tribological performance of laser directed energy deposited Inconel 625 achieved through laser surface remelting, Surf. Coat. Technol. 477 (2024) 130345, https://doi.org/10.1016/j.surfcoat.2023.130345.
[23] C. Wei, H. Ye, Z. Zhao, J. Tang, X. Shen, G. Le, K. Ye, F. Le, Microstructure and fracture behavior of 90W-7Ni-3Fe alloy fabricated by laser directed energy deposition, J. Alloys Compd. 865 (2021) 158975, https://doi.org/10.1016/j.jallcom.2021.158975.
[24] H. Paydas, A. Mertens, R. Carrus, J. Lecomte-Beckers, J. Tchoufang Tchuindjang, Laser cladding as repair technology for Ti–6Al–4V alloy: influence of building strategy on microstructure and hardness, Mater. Des. 85 (2015) 497–510, https://doi.org/10.1016/j.matdes.2015.07.035.
[25] R. Comesaña, F. Quintero, F. Lusquiños, M.J. Pascual, M. Boutinguiza, A. Durán, J. Pou, Laser cladding of bioactive glass coatings, Acta Biomater. 6 (2010) 953–961, https://doi.org/10.1016/j.actbio.2009.08.010.
[26] Y. Estrin, A. Vinogradov, Extreme grain refinement by severe plastic deformation: a wealth of challenging science, Acta Mater. 61 (2013) 782–817, https://doi.org/10.1016/J.ACTAMAT.2012.10.038.

[27] R.Z. Valiev, Y. Estrin, Z. Horita, T.G. Langdon, M.J. Zehetbauer, Y.T. Zhu, Fundamentals of superior properties in bulk nanoSPD materials, Mater Res Lett 3831 (2015) 1–21, https://doi.org/10.1080/21663831.2015.1060543.
[28] A. Azushima, R. Kopp, A. Korhonen, D.Y. Yang, F. Micari, G.D. Lahoti, P. Groche, J. Yanagimoto, N. Tsuji, A. Rosochowski, A. Yanagida, Severe plastic deformation (SPD) processes for metals, CIRP Ann. Manuf. Technol. 57 (2008) 716–735, https://doi.org/10.1016/j.cirp.2008.09.005.
[29] A. Derakhshandeh, H. Shahmir, M. Nili-Ahmadabadi, Microstructure and mechanical properties of ultrafine-grained titanium processed by multi-pass ECAP at room temperature using core–sheath method, J. Mater. Res. 33 (2018) 3809–3817, https://doi.org/10.1557/JMR.2018.291.
[30] P. La, J. Ma, Y.T. Zhu, J. Yang, W. Liu, Q. Xue, R.Z. Valiev, Dry-sliding tribological properties of ultrafine-grained Ti prepared by severe plastic deformation, Acta Mater. 53 (2005) 5167–5173, https://doi.org/10.1016/J.ACTAMAT.2005.07.031.
[31] M. Chegini, A. Fallahi, M.H. Shaeri, Effect of equal channel angular pressing (ECAP) on wear behavior of Al-7075 alloy, Procedia, Mater. Sci. 11 (2015) 95–100, https://doi.org/10.1016/J.MSPRO.2015.11.116.
[32] A.P. Zhilyaev, A. Morozova, J.M. Cabrera, R. Kaibyshev, T.G. Langdon, Wear resistance and electroconductivity in a Cu–0.3Cr–0.5Zr alloy processed by ECAP, J. Mater. Sci. 52 (2017) 305–313, https://doi.org/10.1007/S10853-016-0331-8.
[33] R.B. Figueiredo, E.R. Eduardo, X. Zhao, X. Yang, X. Liu, P.R. Cetlin, T.G. Langdon, Improving the fatigue behavior of dental implants through processing commercial purity titanium by equal-channel angular pressing, Mater. Sci. Eng. A 619 (2014) 312–318, https://doi.org/10.1016/J.MSEA.2014.09.099.
[34] A. Revathi, S. Magesh, V.K. Balla, M. Das, G. Manivasagam, Current advances in enhancement of wear and corrosion resistance of titanium alloys – a review 31 (2016) 696–704, https://doi.org/10.1080/10667857.2016.1212780.
[35] M. Lewandowska, K.J. Kurzydlowski, Recent development in grain refinement by hydrostatic extrusion, J. Mater. Sci. 43 (2008) 7299–7306, https://doi.org/10.1007/s10853-008-2810-z.
[36] Y. Zhang, T. Guo, Q. Li, J. Qin, X. Ding, S. Ye, J. Zhao, Y. Zhou, Novel ultrafine-grained β-type Ti-28Nb-2Zr-8Sn alloy for biomedical applications, J. Biomed. Mater. Res. A 107 (2019) 1628–1639, https://doi.org/10.1002/JBM.A.36679.
[37] C. Jiménez-Marcos, M.S. Baltatu, N.R. Florido-Suárez, P.P. Socorro-Perdomo, P. Vizureanu, J.C. Mirza-Rosca, Mechanical properties and corrosion resistance of two new titanium alloys for orthopaedics applications, Mater Today Proc 72 (2023) 544–549, https://doi.org/10.1016/j.matpr.2022.09.394.
[38] B. Ravisankar, Equal-channel angular pressing (ECAP), in: Handbook of Mechanical Nanostructuring, Wiley-VCH Verlag GmbH & Co. KGaA, Weinheim, Germany, 2015, pp. 277–297, https://doi.org/10.1002/9783527674947.ch13.
[39] P. Kongsuwan, G. Brandal, Y. Lawrence Yao, Laser induced porosity and crystallinity modification of a bioactive glass coating on titanium substrates, J. Manuf. Sci. Eng. 137 (2015) 031004, https://doi.org/10.1115/1.4029566.
[40] M. Roy, B. Vamsi Krishna, A. Bandyopadhyay, S. Bose, Laser processing of bioactive tricalcium phosphate coating on titanium for load-bearing implants, Acta Biomater. 4 (2008) 324–333, https://doi.org/10.1016/j.actbio.2007.09.008.
[41] D. Ke, A.A. Vu, A. Bandyopadhyay, S. Bose, Compositionally graded doped hydroxyapatite coating on titanium using laser and plasma spray deposition for bone implants, Acta Biomater. 84 (2019) 414–423, https://doi.org/10.1016/J.ACTBIO.2018.11.041.
[42] S. Bajda, Y. Liu, R. Tosi, K. Cholewa-Kowalska, M. Krzyzanowski, M. Dziadek, M. Kopyscianski, S. Dymek, A.V. Polyakov, I.P. Semenova, T. Tokarski, Laser cladding of bioactive glass coating on pure titanium substrate with highly refined grain structure, J. Mech. Behav. Biomed. Mater. 119 (2021) 104519, https://doi.org/10.1016/j.jmbbm.2021.104519.
[43] V. Polyakova, I. Semenova, R. Valiev, Influence of annealing on the structure and mechanical properties of ultrafine-grained alloy Ti-6Al-7Nb, processed by severe plastic deformation, Mater. Sci. Forum 667–669 (2011) 943–948, https://doi.org/10.4028/www.scientific.net/msf.667-669.943.
[44] V.V. Polyakova, I.P. Semenova, A.V. Polyakov, D.K. Magomedova, Y. Huang, T. G. Langdon, Influence of grain boundary misorientations on the mechanical behavior of a near-α Ti-6Al-7Nb alloy processed by ECAP, Mater. Lett. 190 (2017) 256–259, https://doi.org/10.1016/j.matlet.2016.12.083.
[45] T. Kokubo, H. Takadama, How useful is SBF in predicting in vivo bone bioactivity? Biomaterials 27 (2006) 2907–2915, https://doi.org/10.1016/j.biomaterials.2006.01.017.
[46] Z. Sun, I. Annergren, D. Pan, T.A. Mai, Effect of laser surface remelting on the corrosion behavior of commercially pure titanium sheet, Mater. Sci. Eng. A 345 (2003) 293–300, https://doi.org/10.1016/S0921-5093(02)00477-X.
[47] L.C. Zhang, H. Attar, Selective laser melting of titanium alloys and titanium matrix composites for biomedical applications: a review, Adv. Eng. Mater. 18 (2016) 463–475, https://doi.org/10.1002/adem.201500419.
[48] P. Kuo, S.S. Joshi, X. Lu, Y. Ho, Y. Xiang, N.B. Dahotre, J. Du, Laser coating of bioactive glasses on bioimplant titanium alloys, Int. J. Appl. Glas. Sci. 10 (2019) 307–320, https://doi.org/10.1111/ijag.12642.
[49] Y. Liu, A. Triantaphyllou, D. Eustice, R. Ireson, C. Holcroft, M. Glendenning, Metal/glass interface metallurgical characterisation of a multiscale bioactive surface structure on Ti-6Al-4V alloy with Laser Cladding, in: World PM2022 Congress Proceedings, European Powder Metallurgy Association (EPMA), Lyon, 2022, ISBN 978-1-899072-55-2.
[50] J. Del Val, R. López-Cancelos, A. Riveiro, A. Badaoui, F. Lusquiños, F. Quintero, R. Comesaña, M. Boutinguiza, J. Pou, On the fabrication of bioactive glass implants for bone regeneration by laser assisted rapid prototyping based on laser cladding, Ceram. Int. 42 (2016) 2021–2035, https://doi.org/10.1016/j.ceramint.2015.10.009.
[51] R. Comesaña, F. Lusquiños, J. Del Val, M. López-Álvarez, F. Quintero, A. Riveiro, M. Boutinguiza, A. De Carlos, J.R. Jones, R.G. Hill, J. Pou, Three-dimensional bioactive glass implants fabricated by rapid prototyping based on CO2laser cladding, Acta Biomater. 7 (2011) 3476–3487, https://doi.org/10.1016/j.actbio.2011.05.023.
[52] F. Lusquiños, F. Arias-González, J. Penide, J. del Val, R. Comesaña, F. Quintero, A. Riveiro, M. Boutinguiza, M.J. Pascual, A. Durán, J. Pou, Laser bioengineering of glass-titanium implants surface, in: M.F.P.C. Martins Costa (Ed.), 8th Iberoamerican Optics Meeting and 11th Latin American Meeting on Optics, Lasers, and Applications, 2013: p. 8785E3. doi:https://doi.org/10.1117/12.2026115.
[53] O. Peitl, E. Dutra Zanotto, L.L. Hench, Highly bioactive P2O5-Na2O-CaO-SiO2glass-ceramics, J. Non-Cryst. Solids 292 (2001) 115–126, https://doi.org/10.1016/S0022-3093(01)00822-5.
[54] L. Peddi, R.K. Brow, R.F. Brown, Bioactive borate glass coatings for titanium alloys, J. Mater. Sci. Mater. Med. 19 (2008) 3145–3152, https://doi.org/10.1007/s10856-008-3419-0.